Atmospheric Research 94 (2009) 37–44

Contents lists available at ScienceDirect

Atmospheric Research

journal homepage: www.elsevier.com/locate/atmos

Statistical representation of equatorial waves and tropical instability waves in the Pacific Ocean

Toshiaki Shinoda [a,*], George N. Kiladis [b], Paul E. Roundy [c]

[a] Center for Ocean-Atmospheric Prediction Studies, Florida State University, Tallahassee, Florida, USA
[b] NOAA Earth System Research Laboratory, Boulder, Colorado, USA
[c] Department of Earth and Atmospheric Sciences, University at Albany, State University of New York, New York, USA

ARTICLE INFO

Article history:
Received 17 March 2008
Received in revised form 4 June 2008
Accepted 23 June 2008

Keywords:
Equatorial waves
Tropical instability waves
Tropical air–sea interaction

ABSTRACT

Sea surface height (SSH), sea surface temperature (SST), and surface currents derived from satellite observations are analyzed to investigate signals of equatorial Kelvin and tropical instability waves (TIWs) in the Pacific Ocean. A wavenumber–frequency spectral analysis of SSH and SST anomalies was performed in order to examine their space and time variability. Significant spectral peaks along the dispersion curves of the first baroclinic mode Rossby and Kelvin waves are found in the SSH spectrum, indicating that the analysis can effectively identify the signals of equatorial waves in the upper ocean. A prominent peak in SSH fields at around 33 days and 1500 km wavelength along the Rossby wave dispersion curve is evident, and a similar peak is also found in SST fields. This upper ocean variability on these space and time scales is shown to be associated with TIWs. The spatial structure of 33-day TIWs is further examined based on an analysis of time series filtered in the frequency-wavenumber domain. The phase relationship between SSH, SST, and surface velocity associated with TIWs is described based on a cross-correlation analysis. Also, the interannual variability of TIW activity is compared with that of ENSO, showing a moderate correlation.

1. Introduction

Equatorially-trapped waves account for a large portion of the intraseasonal variability in the tropical atmosphere and ocean, and play an important role in driving a variety of longer time scale phenomena (e.g., ENSO). Kelvin, Rossby and Mixed Rossby-Gravity waves corresponding to the eigenmodes of the linearized shallow water equations of Matsuno (1966) have been shown to be of particular importance in the equatorial Pacific ocean. While oceanic equatorial waves have been identified in in-situ data (e.g. Johnson and McPhaden, 1993) and in satellite altimeter data (e.g., Miller et al., 1988; Delcroix et al., 1991; Boulanger and Fu 1996; Chelton et al., 2003) their observed dispersion relationships have not yet been fully described in frequency–wavenumber space. A recent study by Wakata (2007) demonstrated that the dispersion relations of equatorial Rossby and Kelvin waves could be inferred from satellite data by frequency–wavenumber spectra of sea surface height (SSH). However, because his analysis includes the background spectrum, it is difficult to compare the spectral signal with theoretical dispersion curves, especially in the high wavenumber domain. In this study, frequency-wavenumber spectral analysis will first be applied to identify observed dispersion relations of oceanic equatorial waves using sea surface height data measured by satellite altimetry.

It is found that signals of oceanic equatorial Kelvin and Rossby waves are evident in the frequency–wavenumber spectrum of SSH. The same analysis is also conducted using sea surface temperature (SST), showing a prominent spectral peak in both SSH and SST at frequencies and wavenumbers consistent with those of tropical instability waves (TIWs). Further statistical analyses are conducted to isolate TIW oceanic

* Corresponding author. Naval Research Laboratory, Stennis Space Center, Mississippi, 39529, USA. Tel.: +1 228 688 5356; fax: +1 228 688 4759.
E-mail address: toshiaki.shinoda@nrlssc.navy.mil (T. Shinoda).

0169-8095/$ – see front matter © 2008 Elsevier B.V. All rights reserved.
doi:10.1016/j.atmosres.2008.06.002

structure and the atmospheric response to TIWs. Interannual variation of TIW activity is also described, and its relation to ENSO is discussed.

2. Data

Five primary data sets are used in this study. 10-day average SSH data derived from TOPEX altimetry are used to identify signals of equatorial waves and TIWs. Data for the 10-year period of 1993–2002 with horizontal resolution of 1° are analyzed. This period includes a strong ENSO cycle (1997/98), and thus the interannual variation of TIW activity in relation to ENSO can be discussed. Weekly SSTs from the analysis of Reynolds et al. (2002) are used to provide a statistical description of SST variability associated with TIWs and to examine the interannual variation of TIW activity. Data for the period 1982–2005 with 1° horizontal resolution are analyzed. The TRMM Microwave Imager (TMI) SST for a period 1998–2005 are also analyzed to describe the structure of TIWs. The 3-day average TMI SST data are originally gridded at 0.25°×0.25°. We average the data onto a 1°×1° grid for comparison with the Reynolds SST. 1° resolution is considered sufficient since the typical wavelength of TIWs is ~1500 km. Near surface velocity data derived from the Ocean Surface Current Analysis-Real time (OSCAR) project (Lagerloef et al., 1999; Bonjean and Lagerloef, 2002) are used to statistically describe the structure of surface current anomalies associated with TIWs. The 5-day average near surface velocity fields on 1°×1° grid are estimated using SSH data from 1999–2005 satellite altimeter measurements, surface wind stress, and drifter data. Surface wind products derived from Quick Scatterometer (QuikSCAT; July 1999–present) measurements are used to describe atmospheric variability associated with TIWs. 6 hourly surface winds with horizontal resolution of 0.5°×0.5° are derived from a space and time blend of QSCAT scatterometer observations and NCEP reanalysis (Milliff et al., 1999; Milliff and Morzel, 2001).

Since the OSCAR velocity is not derived from direct current measurements at each grid point, it is necessary to compare the data with other direct measurements, especially near the equator where geostrophic balance does not necessarily hold. Bonjean and Lagerloef (2002) compared the OSCAR velocity with direct measurements from TOGA TAO buoys for annual and interannual variations, showing that the OSCAR data capture these variations on the equator well, especially in the eastern Pacific. In this study, we also examined the subseasonal variability of OSCAR velocity.

Fig. 1 shows the zonal velocity at 140°W, equator from OSCAR and TAO measurements. The 5-day average zonal velocity at 10 m from TAO measurements is compared with the surface zonal velocity from OSCAR. The OSCAR velocity agrees well with TAO data (correlation coefficient = 0.66) including subseasonal velocity fluctuations associated with strong TIW activity such as was observed during November–December 2001 (Cronin et al., 2003) and August–September 2004 (Jochum et al., 2007). Although there are some significant discrepancies between the two data sets for each individual subseasonal event, the reasonable correlation suggests that the OSCAR velocity data are suitable for the statistical description of TIW structures.

It should be noted that a recent study by Johnson et al. (2007) shows significant errors of meridional velocity near the equator in the OSCAR data. However, the surface currents associated with TIWs statistically derived in our analysis are predominantly zonal near the equator (see Section 4). Hence the error of meridional velocity is not likely to significantly impact the results of the analysis in this particular study.

3. Frequency–wavenumber spectral analysis

Wheeler and Kiladis (1999) demonstrated that wavenumber–frequency spectral analysis is useful for identifying signals of atmospheric equatorial waves, and for isolating their structure. Wavenumber–frequency spectral analysis was also recently used to identify oceanic equatorial waves in numerical model experiments (Shinoda et al., 2008). In this section, the same technique used in Wheeler and Kiladis (1999) is applied to the satellite derived SSH to identify oceanic equatorial waves. In this approach a complex FFT of SSH is first done over longitude to decompose SSH into zonal

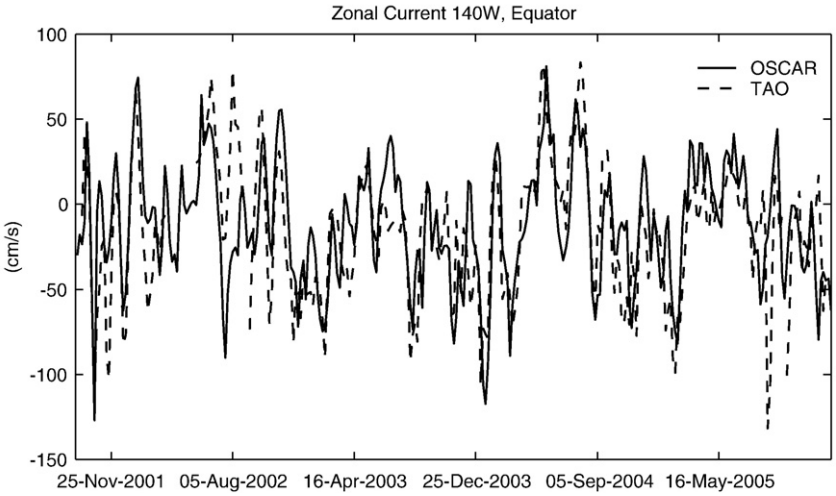

Fig. 1. Time series of surface zonal current at 140°W, equator from OSCAR data (solid line) and 5-day average zonal current at 10 m from the TAO mooring during September 2001–December 2005.

wavenumbers, then an additional FFT is used to determine the spectral power of each resolved wavenumber by frequency. Further details are described by Wheeler and Kiladis (1999).

Fig. 2a shows contours of the base 10 logarithm of power in wavenumber-frequency space calculated using SSH anomalies in the equatorial area (5°N–5°S) in the Pacific Ocean. Despite the red nature of spectrum, some significant peaks along dispersion curves of equatorial waves can be identified. In the positive (eastward) wavenumber domain, prominent spectral signals of the equatorial Kelvin wave are evident, with their peak corresponding to an equivalent depth of 0.8 m and a phase speed of ~2.8 m/s. This phase speed is consistent with that of first baroclinic Kelvin wave in the equatorial Pacific Ocean (e.g., Cravatte et al., 2003; Shinoda et al., 2008). Signals of the second baroclinic mode are also found for a phase speed of around 1.6 m/s, although the signals are very weak. In the negative (westward) wavenumber domain, a spectral peak close to the dispersion curve of the first meridional mode equatorial Rossby wave is evident, at the same equivalent depth as for the 1st mode Kelvin wave.

As with the spectral signals of atmospheric data (Wheeler and Kiladis, 1999), the spectral peaks along the dispersion

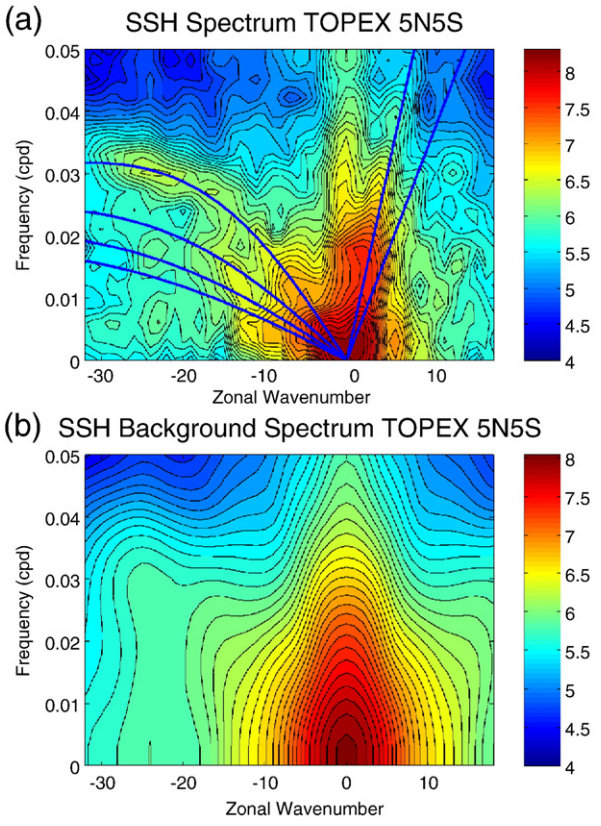

Fig. 2. (a) Zonal wavenumber–frequency power spectrum of SSH anomalies from TOPEX. The number of the color bar indicates the base-10 logarithm. The straight lines indicate 2.8 m/s and 1.6 m/s phase lines, corresponding to equivalent depths of 0.8 m and 0.26 m. Curves in the negative wavenumber domain are Rossby wave dispersion curves of first 4 meridional modes for an equivalent depth of 0.8 m. (b) Zonal wavenumber–frequency spectrum of the "background" power calculated by smoothing the power spectrum of (a). See text for the detail.

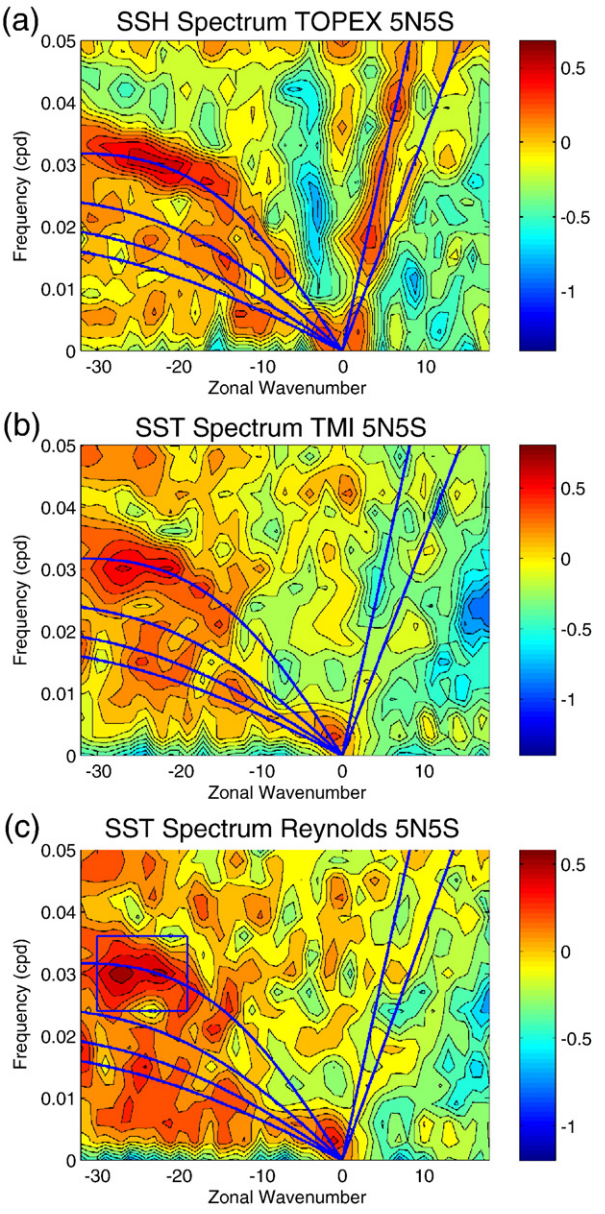

Fig. 3. (a) Zonal wavenumber–frequency power spectrum of SSH anomalies (Fig. 2a) divided by the background (Fig. 2b). The straight and curved lines are dispersion curves as in Fig. 2. (b) Same as (a) except for SST anomalies from TMI. (c) Same as (a) except for Reynolds SST.

curves of oceanic equatorial waves can be found in the raw spectrum of the SSH data, although it is difficult to identify detailed features of the signals especially in the higher wavenumber domain. Hence, following Wheeler and Kiladis (1999), the red background spectrum is calculated, and it is removed from the original spectrum. First, the raw spectra of positive and negative wavenumber domains are averaged to make the spectrum symmetric with regard to the wavenumber 0. Then a 1-2-1 filter is applied multiple times in frequency and wavenumber. Here the number of passes of the 1-2-1 filter is 7 in frequency and 4 in wavenumber. Fig. 2b shows the background spectrum of SSH. The spectrum is red

and relatively smooth, with greatest power at the lowest frequencies and wavenumbers.

The spectral signals without the background are calculated by dividing the power spectrum of Fig. 2a by the background power Fig. 2b (Fig. 3a). Spectral signals of equatorial waves are much more prominent in Fig. 3a than those in Fig. 2a. For example, peaks of similar magnitude along the first baroclinic mode Kelvin wave dispersion line are evident over a wider range of frequency and wavenumber domains. Also, in the negative wavenumber domain, a clear spectral peak along the dispersion curve of the equatorial Rossby wave is evident. In particular, a peak at a period of ~33 days and wave length ~1500 km on the dispersion curves is prominent. These frequencies and wavenumbers are consistent with those associated with TIWs (e.g., Qiao and Weisberg, 1995; Weidman et al., 1999; Lyman et al., 2007). The result is consistent with previous studies which suggest that 33-day TIWs have characteristics similar to an unstable first meridional mode Rossby wave (Lyman et al., 2007). However, because of the existence of strong mean currents in this region, the meridional structure of TIWs is not exactly the same as that of a linear equatorial Rossby wave derived from shallow water equations (e.g., Lyman et al., 2005).

While many previous studies discussed the structure of 33-day period TIWs, Lyman et al. (2007) recently detailed the structure of TIWs with a 17-day period. Although satellite derived SSH data cannot resolve the 17-day period signal, a peak around 17 days could potentially affect the spectrum at longer periods through aliasing. A 33-day spectral peak can be contaminated by aliasing only if there is significant power at ~14 days given that the sampling is 10 days. Since Lyman et al. (2007) show that power less than 15 days is nearly zero (see their Fig. 14), it is unlikely that the 33-day peak is significantly influenced by 17-day signals through aliasing. Also, we have calculated the spectrum using only the northern hemisphere (2°N–5°N) data (not shown), which shows a similar spectral peak. Since the 17-day signal of subsurface temperature is much weaker in the northern hemisphere, we conclude that the 33-day peak is not significantly contaminated by the 17-day signal through aliasing.

Fig. 3b shows the spectrum calculated from the same analysis using the TMI SST. While there is no significant peak near the Kelvin wave dispersion curve, a peak at ~33 days and length ~1500 km is once more evident, suggesting again a spectral signal associated with TIWs. A similar peak is found in the Reynolds SST, showing that a significant portion of TIW variability can be captured by the weekly SST analysis (Fig. 3c).

In order to describe the spatial variation of TIW activity, space and time filtering (via spectral transform) centered around the spectral peak (the area of rectangle in Fig. 3c) is applied to the time series of SSH and SST. Fig. 4a, b and c show the standard deviation of filtered time series at each location from SSH, TMI SST and Reynolds SST respectively. The maximum of SSH fluctuation associated with TIWs is found at 5°N, 130°W, while the maximum in the SST signal is found around 2°N, 120°W (Fig. 4a and b). A similar spatial pattern is found in the analysis of Reynolds SST, but the overall amplitude is weaker (Fig. 4c).

It should be noted that the box shown in Fig. 3c does not completely cover the signal of the SSH spectral peak shown in Fig. 3a. We repeated the same analyses (including those discussed later in Sections 4 and 5) using broader ranges of zonal wavenumbers for filtering. The results vary little from those presented here (not shown), suggesting that results are not sensitive to small changes in the width of the filter box.

4. Cross-correlation analysis

4.1. Structure and evolution of TIWs

Previous observational studies indicate that TIWs are generally associated with strong fluctuations of SST, SSH and near surface currents (e.g., Duing et al., 1975; Legeckis, 1977;

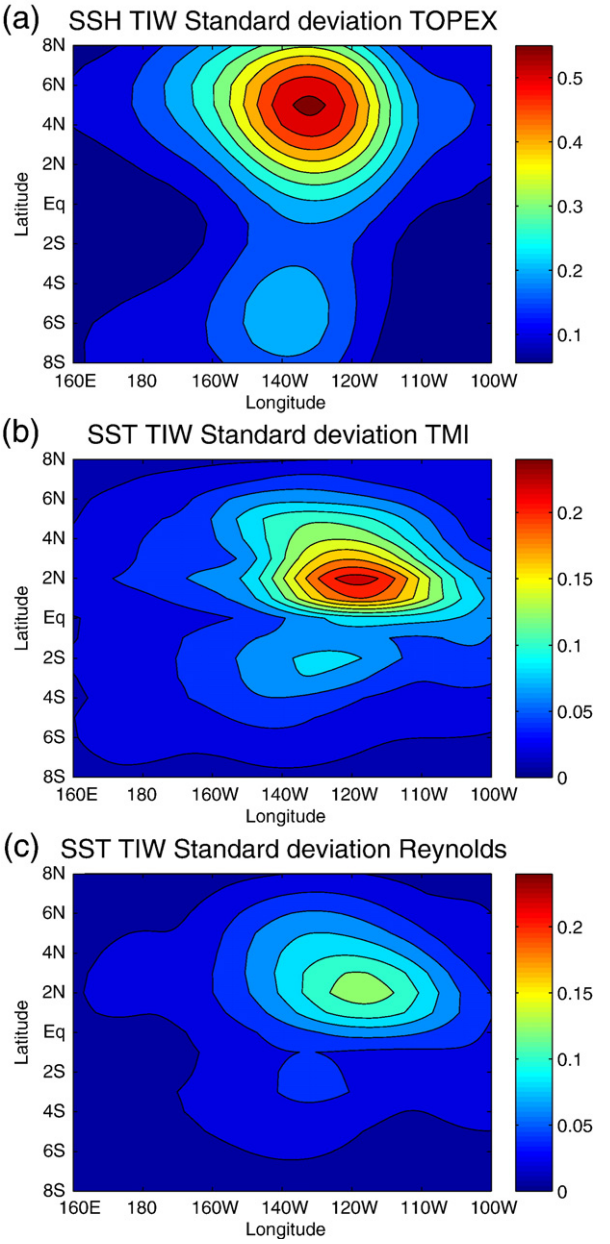

Fig. 4. (a) Standard deviation of SSH anomalies (cm) filtered at periods 28–41 days and wave lengths 1336–2109 km (see the rectangle in Fig. 3c) (b) Same as (a) except for SST anomalies from TMI. (c) Same as (a) except for SST anomalies from Reynolds SST.

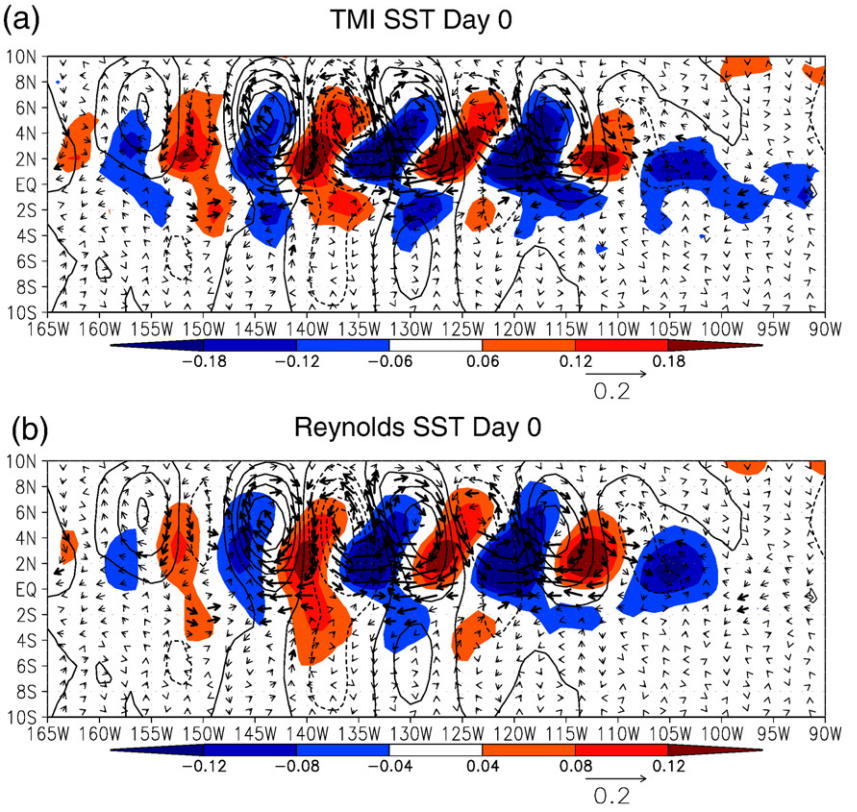

Fig. 5. (a) SST (shading), SSH (contour), and surface current (arrows) anomalies regressed onto space and time filtered SSH anomalies at 5°N, 130°W. TMI SST is used for the analysis. The contour interval is 0.2 cm. The solid (dashed) contour indicates positive (negative) values. Thick arrows indicate velocities larger than 0.03 m/s. (b) Same as the upper panel except Reynolds SST is used.

Miller et al., 1985; Musman, 1989; Kennan and Flament, 2000; Polito et al., 2001; Chelton et al., 2003). In this section, the phase relationships between SST, SSH and surface currents are described statistically using long records based on a cross-correlation analysis.

Time series of unfiltered SSH, SST, and surface current anomalies are regressed against space and time filtered TIW SSH anomalies at 5°N, 130°W where the SSH variance is maximum in Fig. 4a. The data for the period 1999–2002, during which all data sets are available, are used for the analysis.

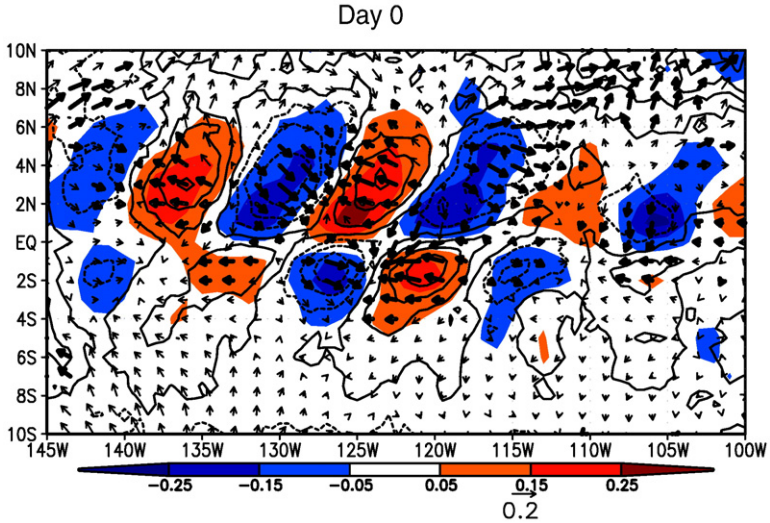

Fig. 6. SST (shading), wind speed (contour), and surface wind (arrows) anomalies regressed onto space and time filtered SST anomalies at 2°N, 120°W. TMI SST is used for the analysis. The contour interval is 0.05 m/s. The solid (dashed) contour indicates positive (negative) values. Thick arrows indicate wind speed larger than 0.05 m/s.

During this period, La Nina conditions were observed in 1999–2000, then a weak El Nino developed in 2002. Fig. 5a shows the relationship of these variables using TMI SST. Maximum SST anomalies are located around 2°N, extending to the northeast. Maximum SSH anomalies are found around 5°N, which corresponds to the local maximum of SST anomalies around this latitude. Surface velocity is found to be almost parallel to the contour lines of SSH, showing nearly geostrophic balance. Because the maximum SSH anomalies are located on the northeast side of the maximum SST anomalies, northward (southward) current anomalies are found at the coldest (warmest) anomalies around 2°N, causing a net meridional heat transport. While these SST anomalies may be initially advected by velocity fluctuations caused by barotropic instability from the cyclonic shear between the South Equatorial Current and North Equatorial Countercurrent or Equatorial Undercurrent (e.g., Qiao and Weisberg, 1995; Contreras, 2002; Chelton et al., 2003), it is possible that variation of the temperature front may influence the evolution of TIWs given that the surface velocity fields are in near geostrophic balance. On the equator, the maximum westward (eastward) currents are found where the zonal gradient of SST anomalies is positive (negative), corresponding to a strong zonal advection of heat. This result is consistent with the analysis of TOGA TAO data (Jochum et al., 2007). The SSH signal is small on the equator, consistent with previous studies (e.g., Musman et al., 1989). These features are also evident in the Reynolds SST, but their amplitude is about 2/3 of that in TMI SST (Fig. 5b).

4.2. Atmospheric response to TIWs

TIWs can significantly influence atmospheric subseasonal variability, which includes surface winds (e.g., Hayes et al., 1989, Xie et al., 1998, Hashizume et al., 2002), clouds and precipitation

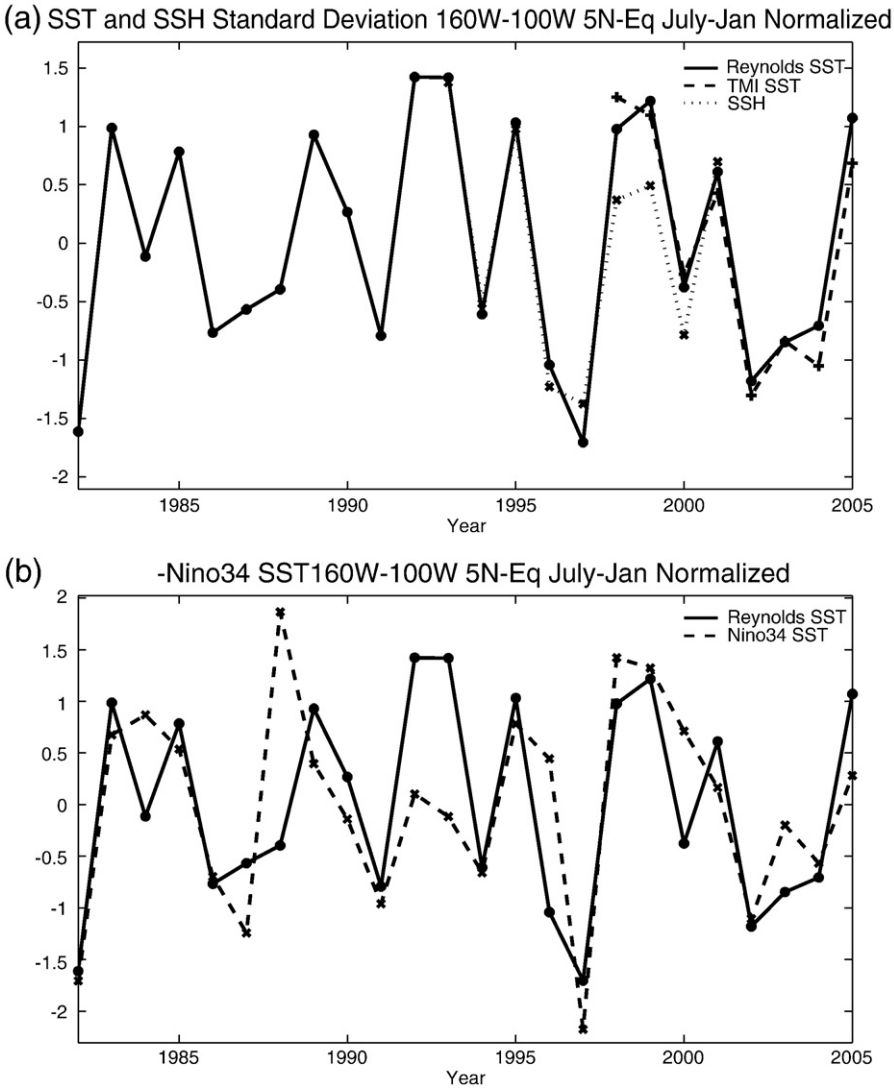

Fig. 7. (a) Variation of the intensity of Reynolds SST (solid line), TMI SST(dashed line), and SSH (dotted line) associated with TIW for the area 160°W–100°W, 5°N–0°. The intensity of these variables are measured by the standard deviation of space and time filtered time series during July–January in each year. (b) The solid line is same as in (a). The dashed lines is the time series of Nino3.4 SST averaged for the same season as in (a). The sign of Nino3.4 SST is reversed for the comparison.

(Deser et al., 1993, Hashizume et al., 2001), surface heat flux (Thum et al., 2002), and near surface pressure (e.g., Cronin et al., 2003). In order to statistically describe the atmospheric response to TIWs using a long record, similar regression analyses as above have been conducted using scatterometer wind data.

Surface winds and wind speed from QSCAT data during the period 1999–2002 are regressed against the filtered TMI SST at 2°N, 120°W where the amplitude of SST associated with TIWs is maximum (Fig. 4b). Fig. 6 shows the regressed surface winds and wind speed along with the regressed SST anomalies. Southeasterly (northwesterly) anomalies are found in the area of warm (cold) SST anomalies associated with TIWs. This spatial pattern of winds is consistent with previous studies using a short record (e.g., Hashizume et al., 2002). Since the mean winds in the eastern equatorial Pacific are easterly in most areas, easterly (westerly) anomalies in the warm (cold) SST areas enhance (reduce) the total wind speed. Therefore the wind speed is found to be enhanced in the area of warm SST anomalies and reduced in the cold SST anomalies.

This spatial pattern of wind speed could cause a negative feedback through the latent heat flux associated with TIWs. Evaporative cooling tends to be larger in the area of warm SST. Higher wind speeds in regions of warmer SST implies that evaporative cooling is more enhanced by surface winds induced by TIWs.

5. Interannual variation of TIWs

The results in previous sections indicate that major features of SST variability associated with TIWs can be well captured by Reynolds SST based on a comparison with those from TMI SST. Because the Reynolds SST covers a much longer period, it is useful to examine the interannual variation of TIW activity inferred by that data set. In this section, interannual variation of TIW activity derived from Reynolds SST is first compared with that from TMI SST and SSH in recent years. Then the longer time series of TIW activity from the Reynolds SST is compared with an ENSO index time series.

The intensity of TIW activity is measured as the standard deviation of the space and time filtered time series for July–January periods, when TIWs are most active. Fig. 7a shows the intensity of TIW activity in each year measured by the standard deviation of filtered SSH, TMI SST and Reynolds SST for the area 160°W–100°W, 5°N–0°, where strong TIWs are observed. The year-to-year variation of the intensity from the Reynolds SST is similar to that from TMI SST when the time series amplitudes are normalized. The intensity of SSH is also similar to that from Reynolds and TMI SST.

Fig. 7b compares the TIW activity calculated from Reynolds SST using the Nino 3.4 SST, an index of ENSO, for the same period. TIW activity tends to be strong during La Nina, which is consistent with previous work in which several examples of TIWs during El Nino and La Nina periods are described (Contreras, 2002). However, these time series do not show strong one-to-one relationships between the two, and the correlation is fairly modest (correlation coefficient = 0.64). In fact, the strongest activity during this period is observed in 1992 and 1993 when Nino 3.4 SST is nearly normal. This suggests that factors besides ENSO are important for controlling the TIW activity. We have also compared the TIW activity with the meridional shear of the surface zonal current and the meridional SST gradient near 2°N. However, these time series are similar to Nino 3.4 SST (not shown), and thus the correlations with TIW activity are also similar.

6. Conclusions

Satellite derived SSH, SST and surface velocity are analyzed to examine oceanic equatorial waves and tropical instability waves. Signals of oceanic equatorial waves can be isolated by frequency–wavenumber spectral analysis of SSH fields derived from satellite altimeter measurements. A prominent peak at around a 33 day period and a wavelength of around 1500 km is found to be associated with TIWs, and this peak corresponds to that of 1st meridional mode equatorial Rossby waves with an equivalent depth 0.8 m. Salient features of TIWs such as phase relationships between surface velocity, SSH, and SST can be effectively isolated by a combination of frequency–wavenumber spectral analysis and regression. These statistical description of TIWs should be useful for evaluating model performance in simulating TIWs, since models generally do not do well simulating individual TIWs.

Interannual variability of TIW activity is further examined using these data sets. It is found that TIW activity for the most part tends to be more intense during La Nina and weak in El Nino, but there are some remarkable exceptions. For example, during 1992–93, TIWs are found to be very active while the Nino 3.4 SST is near normal, suggesting that other factors are also important for controlling the interannual variation of TIW activity.

Acknowledgments

The TAO Project Office of NOAA/PMEL provided the mooring time series data. The TMI data are obtained from the Remote Sensing Systems web site. TOPEX data are obtained from the Center for Space Research, University of Texas at Austin. Constructive comments by two reviewers helped improve the original draft of this paper. Toshiaki Shinoda is supported by NOAA CLIVAR-Pacific Grant from Office of Global Programs, NSF Grant OCE-0453046, and the 6.1 project Global Remote Littoral Forcing via Deep Water Pathways sponsored by the Office of Naval Research (ONR) under program element 601153N. George Kiladis is supported by NOAA's Climate Program Office under grant GC05-156. Paul Roundy is supported by start-up funds from the Research Foundation for the State University of New York.

References

Bonjean, F., Lagerloef, G.S.E., 2002. Diagnostic model and analysis of the surface currents in the Tropical Pacific ocean. J. Phys. Oceanogr. 32, 2938–2954.

Boulanger, J.P., Fu, L.L., 1996. Evidence of boundary reflection of Kelvin and first-mode Rossby waves from TOPEX/POSEIDON sea level data. J. Geophys. Res. 101, 16361–16371.

Chelton, D.B., Schlax, M.G., Lyman, J.M., Johnson, G.C., 2003. Equatorially trapped Rossby waves in the presence of meridionally sheared baroclinc flow in the Pacific Ocean. Prog. Oceanogr. 56, 323–380.

Contreras, R.F., 2002. Long-term observations of tropical instability waves. J. Phys. Oceanogr. 32, 2715–2722.

Cravatte, S., Picaut, J., Eldin, G., 2003. Second and first baroclinic Kelvin modes in the equatorial Pacific at intraseasonal time scales. J. Geophys. Res. 108 (22), 1–20.

Cronin, M.F., Xie, S.P., Hashizume, H., 2003. Barometric pressure variations associated with eastern Pacific tropical instability waves. J. Climate 16, 3050–3057.

Delcroix, T., Picaut, J., Eldin, G., 1991. Equatorial Kelvin and Rossby wave evidenced in the Pacific Ocean through Geosat sea level and surface current anomalies. J. Geophys. Res. 96, 3249–3262.
Deser, C., Bates, J.J., Wahl, S., 1993. The influence of sea surface temperature on stratiform cloudiness along the equatorial front in the Pacific Ocean. J. Climate 6, 1172–1180.
Duing, W., Hisard, P., Katz, E., Knauss, J., Meincke, J., Miller, L., Moroshkin, K., Philander, G., Rybnikov, A., Voigt, K., Weisberg, R., 1975. Meanders and longwaves in the equatorial Atlantic. Nature 257, 280–284.
Hashizume, H., Xie, S.P., Liu, W.T., Takeuchi, K., 2001. Local and remote atmospheric response to tropical instability waves: a global view from space. J. Geophys. Res. 106, 10173–10185.
Hashizume, H., Xie, S.P., Fujitani, M., Shiotani, M., Watanabe, T., Tanimoto, Y., Liu, W.T., Takeuchi, K., 2002. Direct observations of atmospheric boundary layer response to SST variations associated with tropical instability waves over the eastern equatorial Pacific. J. Climate 15, 3379–3393.
Hayes, S.P., McPhaden, M.J., Wallace, J.M., 1989. The influence of sea surface temperature on surface wind in the eastern equatorial Pacific. J. Climate 2, 1500–1506.
Jochum, M., Cronin, M.F., Kessler, W.S., Shea, D., 2007. Observed horizontal temperature advection by tropical instability waves. Geophys. Res. Lett. 34, L09604. doi:10.1029/2007GL029416.
Johnson, E.S., McPhaden, M.J., 1993. Structure of intraseasonal Kelvin waves in the equatorial Pacific Ocean. J. Phys. Oceanogr. 23, 608–625.
Johnson, E.S., Bonjean, F., Lagerloef, G.S., Gunn, J.T., Michum, G.T., 2007. Validation and error analysis of OSCAR sea surface currents. J. Atmos. Ocean. Technol. 24, 688–701.
Kennan, S.C., Flament, P., 2000. Observations of tropical instability vortex. J. Phys. Oceanogr. 30, 2277–2301.
Lagerloef, G.S.E., Mitchum, G.T., Lukas, R., Niiler, P.P., 1999. Tropical Pacific near Surface Currents estimated from altimeter, wind and drifter data. J. Geophys. Res. 104 23 313–23 326.
Legeckis, R.V., 1977. Long waves in the eastern equatorial ocean. Science 197, 1177–1181.
Lyman, J.M., Chelton, D.B., deSzoeke, R.A., Samelson, R.M., 2005. Tropical instability waves as a resonance between equatorial Rossby waves. J. Phys. Oceanogr. 17, 232–253.
Lyman, J.M., Johnson, G.C., Kessler, W.S., 2007. Distinct 17- and 33-day tropical instability waves in subsurface observations. J. Phys. Oceanogr. 37, 855–872.
Matsuno, T., 1966. Quasi-geostrophic motions in the equatorial area. J. Meteor. Soc. Jpn 44, 25–43.
Miller, L., Watts, D.R., Wimbush, M., 1985. Oscillations of dynamic topography in the eastern Pacific. J. Phys. Oceanogr. 15, 1759–1770.
Miller, L., Cheney, R., Douglas, B., 1988. GEOSAT altimeter observations of Kelvin waves and the 1986–87 El Nino. Science 239, 52–54.
Milliff, R.F., Morzel, J., 2001. The global distribution of the time-average wind stress curl from NSCAT. J. Atmos. Sci. 58, 109–131.
Milliff, R.F., Large, W.G., Morzel, J., Danabasoglu, G., Chin, T.M., 1999. Ocean general circulation model sensitivity to forcing from scatterometer winds. J. Geophys. Res. 104, 11337–11358.
Musman, S., 1989. Sea height wave form in equatorial waves and its interpretation. J. Geophys. Res. 94, 3303–3309.
Polito, P.S., Ryan, J.P., Liu, W.T., Chavez, F.P., 2001. Oceanic and atmospheric anomalies of tropical instability waves. Geophys. Res. Lett. 28, 2233–2236.
Qiao, L., Weisberg, R.H., 1995. Tropical instability wave kinematics: observations from the Tropical Instability Wave Experiment (TIWE). J. Geophys. Res. 100, 8677–8693.
Reynolds, R.W., Rayner, N.A., Smith, T.M., Stokes, D.C., Wang, W., 2002. An improved in situ and satellite SST analysis for climate. J. Climate 15, 1609–1625.
Shinoda, T., Roundy, P.E., Kiladis, G.N., 2008. Variability of intraseasonal Kelvin waves in the equatorial Pacific Ocean. J. Phys. Oceanogr. 38, 921–944.
Thum, N.S., Esbensen, K., Chelton, D.B., McPhaden, M.J., 2002. Air–sea heat exchange along the northern sea surface temperature front in the eastern tropical Pacific. J. Climate 15, 3361–3378.
Wakata, Y., 2007. Frequency–wavenumber spectra of equatorial waves detected from satellite altimeter data. J. Oceanogr. 63, 483–490.
Weidman, P.D., Mickler, D.L., Dayyani Et, B., Born, G.H., 1999. Analysis of Legeckis eddies in the near-equatorial Pacific. J. Geophys. Res. 104, 7865–7887.
Wheeler, M., Kiladis, G.N., 1999. Convectively coupled equatorial waves: Analysis of clouds and temperature in the wavenumber-frequency domain. J. Atmos. Sci. 56, 374–399.
Xie, S.P., Ishiwatari, M., Hashizume, H., Takeuchi, K., 1998. Coupled ocean-atmospheric waves on the equatorial front. Geophys. Res. Lett. 25, 3863–3866.